

ms time constant of a micrometer-sized electrode (18) (having a large counterelectrode) suggests that very high-frequency operation may be achievable for single nanotube actuators, this remains to be experimentally demonstrated. Our nanotube actuators are first prototypes, and much more work is required before the potential advantages of this technology can be experimentally assessed in practical devices.

Nevertheless, relatively modest improvements in the presently demonstrated actuator properties may enable such applications as electrically activated microcantilevers for medical catheter applications, where a low operation voltage is a major advantage. Using high-temperature electrolytes (molten or solid state), it may be possible to make nanotube actuators that function at temperatures far above those usable for ferroelectrics, which might be important for such applications as airflow control in jet engines. Also, demonstrations of nanotube actuator operation in seawater and in saline solutions, which are electrochemically like blood, suggest various possible marine and biomedical applications. Finally, nanotube actuators could be run in reverse to convert mechanical energy to electrical energy for mechanical sensor and energy-conversion devices. Ferroelectrics generate low currents at high voltages, but the nanotubes would provide high currents at low voltages. This effect is desirable for minimizing the effect of lead capacitances for remotely located sensors; for example, so that sensor-response amplifiers need not be located down-hole when doing seismology for oil exploration. If nanotubelike mechanical properties can be exploited to provide large inputs of mechanical energy, the output volumetric (or gravimetric) electrical energy per cycle would be much higher than that produced by alternative technologies. This feature, as well as the feasibility of operation at low frequencies, may eventually enable such applications as the conversion of the mechanical energy of ocean waves to electrical energy.

References and Notes

1. R. H. Baughman, L. W. Shacklette, R. L. Elsenbaumer, E. J. Plichta, C. Becht, in *Conjugated Polymeric Materials: Opportunities in Electronics, Optoelectronics, and Molecular Electronics*, J. L. Bredas and R. R. Chance, Eds., vol. 182 of NATO ASI Series E: Applied Sciences (Kluwer, Dordrecht, Netherlands, 1990), pp. 559–582; R. H. Baughman, *Synth. Met.* **78**, 339 (1996).
2. E. Smela, O. Inganäs, I. Lundström, *Science* **268**, 1735 (1995); T. F. Otero and J. M. Sansinena, *Adv. Mater.* **10**, 491 (1998); A. Della Santa, D. De Rossi, A. Mazzoldi, *Smart Mater. Struct.* **6**, 23 (1997); M. R. Gandhi, P. Murray, G. M. Spinks, G. G. Wallace, *Synth. Met.* **73**, 247 (1995); J. D. Madden, P. G. Madden, I. W. Hunter, S. R. Lafontaine, C. J. Brennan, in *Proceedings—Workshop on Working in the Micro-World*, IEEE IROS96, Osaka, Japan, November 1996 (IEEE, New York, 1996), pp. 9–18.
3. K. Kaneto, M. Kaneko, Y. Min, A. G. MacDiarmid, *Synth. Met.* **71**, 2211 (1995).
4. J. Liu et al., *Science* **280**, 1253 (1998); A. G. Rinzler et al., *Appl. Phys. A* **67**, 29 (1998).
5. L. Pietronero and S. Strässler, *Phys. Rev. Lett.* **47**, 593 (1981); M. Kertesz, *Mol. Cryst. Liq. Cryst.* **126**, 103

- (1985); C. T. Chan, W. A. Kamitakahara, K. M. Ho, P. C. Eklund, *Phys. Rev. Lett.* **58**, 1528 (1987); R. H. Baughman, N. S. Murthy, H. Eckhardt, M. Kertesz, *Phys. Rev. B* **46**, 10515 (1992).
6. D. E. Nixon and G. S. Perry, *J. Phys. C Solid State Phys.* **2**, 1732 (1969); Y. Murakami, T. Kishimoto, H. Suematsu, *J. Phys. Soc. Jpn.* **59**, 571 (1990); J. E. Fisher, H. J. Kim, V. B. Cajipe, *Phys. Rev. B* **36**, 4449 (1987); W. A. Kamitakahara, J. L. Zaretsky, P. C. Eklund, *Synth. Met.* **12**, 301 (1985); F. Baron, S. Flandrois, C. Hauw, J. Gaultier, *Solid State Commun.* **42**, 759 (1982); S. Flandrois, C. Hauw, R. B. Mathur, *Synth. Met.* **34**, 399 (1990).
7. J. A. Spudich, *Nature* **372**, 515 (1994).
8. E. W. Wong, P. E. Sheehan, C. M. Leber, *Science* **273**, 1971 (1997); M. R. Falvo et al., *Nature* **389**, 582 (1997).
9. The SWNTs were commercially obtained as an aqueous suspension from Tubes@Rice (Rice Univ., Houston, TX). The nanotube sheets were typically made by vacuum filtration of ~20 ml of a ~0.6 mg/ml nanotube suspension through a poly(tetrafluoroethylene) filter (Millipore LS, 47 mm in diameter, 5-µm pores). The nanotube sheet (formed over the clear funnel area, which was 37 mm in diameter) was washed with ~200 ml of deionized water and then 100 ml of methanol to remove residual NaOH and surfactant, respectively. These sheets were allowed to dry under continued vacuum purge for ~1 hour before being peeled from the filter. The typical nanotube sheet was between 15 and 35 µm thick and

- weighed ~12 mg, providing a bulk density of 0.3 to 0.4 g/cm<sup>3</sup> and a four-point probe electrical conductivity of ~5000 S/cm.
10. A. Thess et al., *Science* **273**, 483 (1996).
11. Y. Ye et al., *Appl. Phys. Lett.* **74**, 2307 (1999).
12. J.-P. Radin and E. Yeager, *Electroanal. Chem. Interfacial Electrochem.* **36**, 257 (1972); H. Gerischer, R. McIntyre, D. Scherson, W. Storck, *J. Phys. Chem.* **91**, 1930 (1987); Y. Oren, I. Glatt, A. Livnat, O. Kafri, A. Soffer, *J. Electroanal. Chem.* **187**, 59 (1985).
13. A. M. Rao, P. C. Eklund, S. Bandow, A. Thess, R. E. Smalley, *Nature* **388**, 257 (1997).
14. R. H. Baughman et al., unpublished data.
15. G. Gao, T. Çagin, W. A. Goddard, *Nanotechnology* **9**, 184 (1998); M. M. J. Treacy, T. W. Ebbesen, J. M. Gibson, *Nature* **381**, 678 (1996); E. W. Wong, P. E. Sheehan, C. M. Lieber, *Science* **277**, 1971 (1997).
16. Q. M. Zhang, V. Bharti, X. Zhao, *Science* **280**, 2101 (1998).
17. K. Uchino, *Piezoelectric Actuators and Ultrasonic Motors* (Kluwer Academic, Boston, 1997).
18. R. J. Forster, *Chem. Soc. Rev.* **23**, 289 (1994).
19. We thank J. Su, W. Kuhn, V. Z. Vardeny, L. Dalton, R. Duran, L. Grigorian, and P. C. Eklund for discussions and other valuable contributions. Partially supported by Defense Advanced Research Projects Agency grant N00173-99-2000.

2 February 1999; accepted 9 April 1999

# The Magnetic Excitation Spectrum and Thermodynamics of High-*T<sub>c</sub>* Superconductors

Pengcheng Dai,<sup>1\*</sup> H. A. Mook,<sup>1</sup> S. M. Hayden,<sup>2</sup> G. Aeppli,<sup>3</sup> T. G. Perring,<sup>4</sup> R. D. Hunt,<sup>5</sup> F. Doğan<sup>6</sup>

Inelastic neutron scattering was used to study the wave vector- and frequency-dependent magnetic fluctuations in single crystals of superconducting YBa<sub>2</sub>Cu<sub>3</sub>O<sub>6+x</sub>. The spectra contain several important features, including a gap in the superconducting state, a pseudogap in the normal state, and the much-discussed resonance peak. The appearance of the pseudogap determined from transport and nuclear resonance coincides with formation of the resonance in the magnetic excitations. The exchange energy associated with the resonance has the temperature and doping dependences as well as the magnitude to describe approximately the electronic specific heat near the superconducting transition temperature (*T<sub>c</sub>*).

The parent compounds of the high transition temperature (high-*T<sub>c</sub>*) cuprate superconductors are antiferromagnetic (AF) insulators characterized by a simple doubling of the crystallographic unit cells in the CuO<sub>2</sub> planes. When holes are doped into these planes, the long-range AF-ordered phase disappears and the lamellar cop-

per oxide materials become metallic and superconducting with persistent short-range AF spin correlations (fluctuations). Although spin fluctuations in cuprate superconductors are observed for materials such as YBa<sub>2</sub>Cu<sub>3</sub>O<sub>6+x</sub> [denoted as (123)O<sub>6+x</sub>] at all hole-doping levels, *x* (1–6), the role of such fluctuations in the pairing mechanism and superconductivity is still a subject of controversy (7). The most prominent feature in the fluctuations for (123)O<sub>6+x</sub> is a sharp resonance, which for highly doped compositions appears below the superconducting transition temperature *T<sub>c</sub>* at an energy of 41 meV (1–3). We show that the temperature-dependent resonance intensity is correlated with the electronic part of the specific heat of (123)O<sub>6+x</sub>, *C<sup>el</sup>(*x*, *T*)* (8, 9), including the extended fluctuation regime (“pseudogap phase”), and that the pseudogap temperature *T\** deter-

<sup>1</sup>Solid State Division, Oak Ridge National Laboratory, Oak Ridge, TN 37831–6393, USA. <sup>2</sup>H. H. Wills Physics Laboratory, University of Bristol, Bristol BS8 1TL, UK. <sup>3</sup>NEC Research Institute, 4 Independence Way, Princeton, NJ 08540, USA. <sup>4</sup>Rutherford Appleton Laboratory, Chilton, Didcot, OX11 0QX, UK. <sup>5</sup>Chemical Technology Division, Oak Ridge National Laboratory, Oak Ridge, TN 37831–6221, USA. <sup>6</sup>Department of Materials Science and Engineering, University of Washington, Seattle, WA 98195, USA.

\*To whom correspondence should be addressed. E-mail: piq@ornl.gov

## REPORTS

mined from the onset of the resonance intensity agrees with results of transport and nuclear magnetic resonance (NMR) techniques. By making absolute intensity measurements of the magnetic resonance,  $S_{res}(q,\omega)$ , we estimate the contribution of its exchange energy (10, 11) to the  $C^{el}(x,T)$  anomaly around  $T_c$ . We find that the temperature and doping dependence of the resonance exchange energy can account for the  $C^{el}(x,T)$  anomaly (9), suggesting that a large part of this anomaly is due to spin fluctuations.

Our experiments were performed using triple-axis spectrometers at the High-Flux Isotope Reactor (HFIR) of the Oak Ridge National Laboratory (2, 4) and the MARI direct geometry chopper spectrometer at the ISIS pulsed spallation neutron source of the Rutherford Appleton Laboratory (12). The momentum transfer ( $q_x, q_y, q_z$ ) is measured in units of  $\text{\AA}^{-1}$  and reciprocal space positions are specified in reciprocal lattice units (rlu) ( $h, k, l$ ) = ( $q_x a/2\pi, q_y b/2\pi, q_z c/2\pi$ ), where  $a, b$  ( $\approx a$ ), and  $c$  are the lattice parameters of the orthorhombic unit cell of  $(123)\text{O}_{6+x}$ . For this study, we prepared four single-crystal samples by the melt texture growth technique (2, 4). Subsequent annealing resulted in oxygen stoichiometries of  $x = 0.6, 0.7, 0.8,$  and  $0.93$  with superconducting transitions at  $T_c = 62.7, 74, 82,$  and  $92.5$  K, respectively.

The complete magnetic excitation spectra (Fig. 1) are obtained by integration of the magnetic neutron scattering over the two-dimensional Brillouin zone (BZ) of  $(123)\text{O}_{6+x}$  for  $x = 0.6$  at several temperatures (13, 14). Because the  $\text{CuO}_2$  planes in  $(123)\text{O}_{6+x}$  actually appear in coupled bilayers, magnetic fluctua-

tions that are in-phase (acoustic or  $\chi''_{ac}$ ) or out-of-phase (optical or  $\chi''_{op}$ ) (15) with respect to the neighboring plane will have different spectra (1–6). That the optical excitations occur at higher energies than the acoustic excitations, and are characterized by a substantial gap even in the normal state at 80 K, demonstrates that the bilayer coupling remains antiferromagnetic on going from the insulating parent to the superconducting metal. Upon lowering the temperature from 290 to 35 K, the most dramatic change in the local-susceptibility  $\chi''(\omega)$  for energies less than 100 meV is the appearance of a resonance at 34 meV in the acoustic mode, as shown in the shaded areas of Fig. 1. For  $x = 0.6$ , the resonance is present not only below  $T_c$  but also at 80 K, albeit in reduced form. Beyond the resonance, there is a broad feature extending at least to 220 meV, with a maximum at approximately 75 meV. This broad feature is reminiscent of the continuum, peaked at around 20 meV, seen in the single-layer compound  $\text{La}_{1.86}\text{Sr}_{0.14}\text{CuO}_4$  (16). Well below the resonance peak, scattering is suppressed and a true spin-gap with a value of about 20 meV develops in the superconducting state (Fig. 1A). At room temperature, the optical and acoustic spectra (Fig. 1, C and F) show no maxima over the range of our measurements.

Because the most dramatic change in the magnetic spectrum is the change in the resonance intensity, we focused on the temperature and composition dependence of the resonance. The detailed momentum and frequency dependence of  $S_{res}(q,\omega)$  obtained at HFIR at various temperatures around the resonance energy for  $(123)\text{O}_{6.6}$  (Fig. 2) show that in the low-temper-

ature superconducting state (Fig. 2A), the spectrum is dominated by the resonance at 34 meV. At temperatures just above  $T_c$  (Fig. 2B), the resonance broadens and decreases in intensity, consistent with the ISIS data of Fig. 1. The resonance peak intensity appears to shift smoothly toward higher energies in the normal state with increasing temperature. A signature of the resonance remains at 125 and 150 K, but essentially vanishes at 200 K. Previous temperature-dependent measurements for underdoped  $(123)\text{O}_{6+x}$  indicate that the resonance peak intensity changes its characteristics at  $T_c$  (4, 5). Whereas the intensity at the resonance energy has a noticeable upturn upon cooling through  $T_c$ , the scattering at frequencies above and below the resonance decrease below  $T_c$  (4, 5).

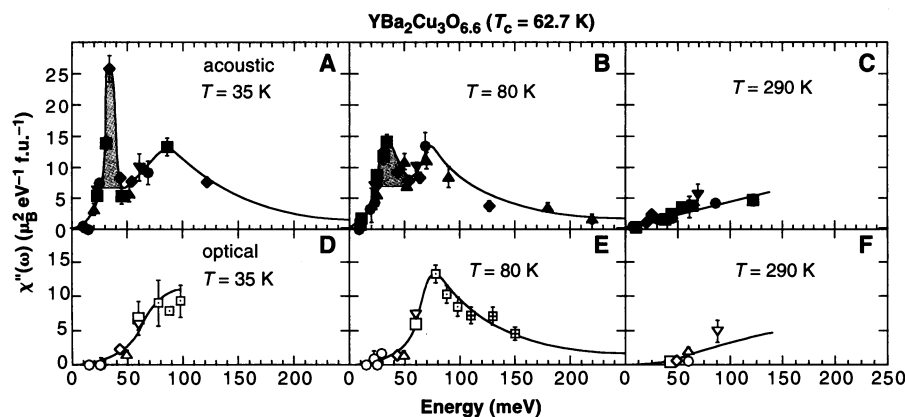


**Fig. 1.** Local- or wave vector-integrated frequency-dependent magnetic susceptibility  $\chi''(\omega)$  for acoustic and optical modes in  $(123)\text{O}_{6.6}$  corrected for the isotropic  $\text{Cu}^{2+}$  magnetic form factor and instrumental resolution (13). The effect of  $\text{Cu}^{2+}$  anisotropic form factor (27) is not considered. The data were collected with the crystal mounted in the  $(h,h,l)$  scattering plane at the MARI spectrometer at ISIS. (A through C) were chosen at  $q_z$  positions to emphasize acoustic modes, and (D through F) emphasize the optical modes. Integrating the area under the resonance peak and converting to moment squared yields  $\langle m_{res}^2 \rangle = 0.06 \pm 0.04 \mu_B^2 \text{f.u.}^{-1}$  at 35 K and  $0.04 \pm 0.03 \mu_B^2 \text{f.u.}^{-1}$  at 80 K. The resonance in  $(123)\text{O}_{6.6}$  accounts for about 14% of the spectral weight up to 80 meV at 35 K (Fig. 1A) and about 1% of the total moment-squared  $2g^2 \mu_B^2 S(S+1) = 6 \mu_B^2$  expected per formula unit (f.u.), assuming  $S = 1/2$  for each Cu ion. Similarly, we found that the 41-meV resonance for  $(123)\text{O}_{6.93}$  has  $\langle m_{res}^2 \rangle = 0.06 \pm 0.04 \mu_B^2 \text{f.u.}^{-1}$  at 25 K. Note that the estimated error in  $\langle m_{res}^2 \rangle$  does not include the  $\sim 30\%$  systematic error involved in normalizing the scattering to a vanadium standard.

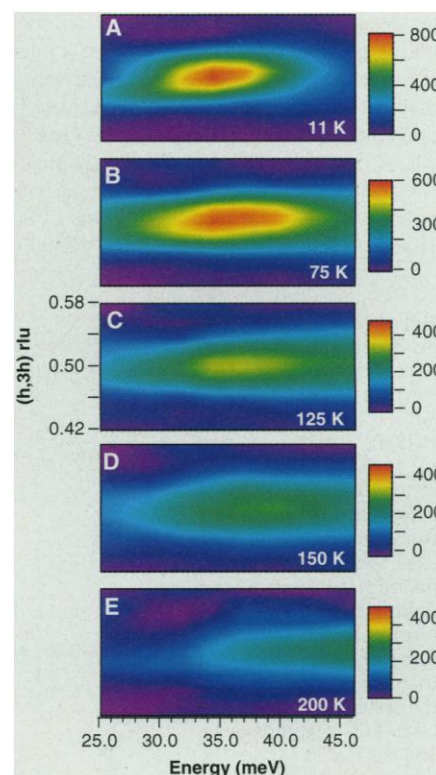


**Fig. 2.** The magnetic structure factor  $S_{res}(q,\omega)$  around the resonance energy for  $(123)\text{O}_{6.6}$  at various temperatures. The data were taken with the HB-3 triple-axis spectrometer at HFIR using pyrolytic graphite as monochromator, analyzer, and filters. The collimations were (proceeding from the reactor to the detector)  $50^\circ\text{-}40^\circ\text{-}80^\circ\text{-}240^\circ$ , and the final neutron energy was fixed at 30.5 meV. To compose the color figures, constant-energy scans along the  $(h,3h,1.7)$  direction (3, 4) from  $h = 0.42$  to  $0.58$  rlu were performed at energy transfers of  $\hbar\omega = 25, 27, 30, 34, 37, 40, 43,$  and  $46$  meV. Magnetic intensity was assumed to be scattering above the linear background of the constant-energy scans. The scattering at different temperatures was normalized to 300 monitor counts, which corresponds to 7 min per point at  $\hbar\omega = 34$  meV. Note the change in the vertical color bar scales, made to better display the marked decrease of the magnetic intensities on warming.

## REPORTS

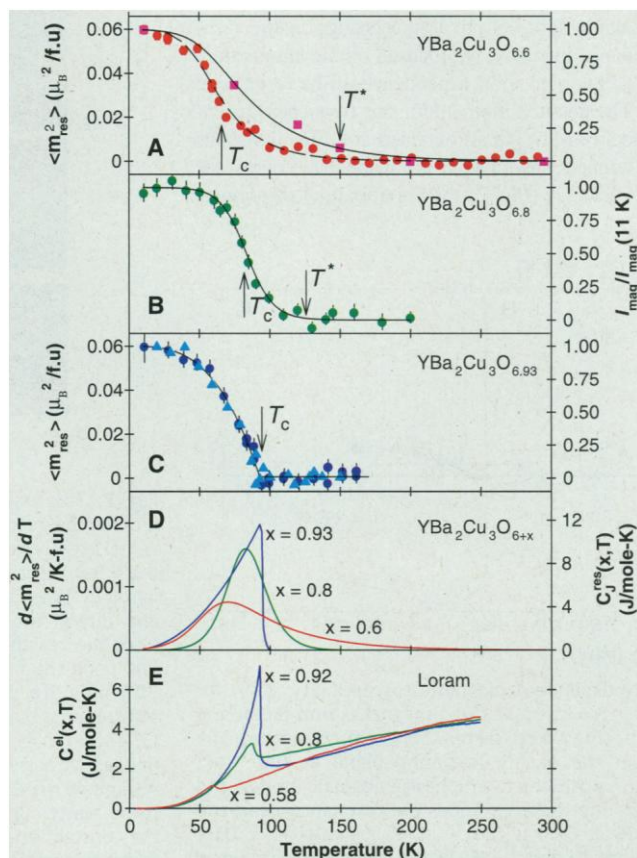
This behavior can now be understood as arising from the narrowing of the resonance in energy from the normal to the superconducting states.

The temperature dependence of the resonance peak intensity [ $S_{res}(q,\omega)$ ] for three (123) $O_{6+x}$  samples with different doping levels and transition temperatures is shown in Fig. 3, A through C. For  $x = 0.6$ , the temperature dependence of the momentum- and frequency-integrated resonance is found to be different from that of the peak intensity (Fig. 3A). For (123) $O_{6.8}$ , similar behavior also occurs, but because the resonance is weaker above  $T_c$ , the counting times required to obtain reliable integrals of the type found for  $x = 0.6$  are prohibitive, and so we are content with simply plotting the peak intensities. Finally, for  $x = 0.93$ , no broadening in either energy or wave vector has been identified (1–3), and so in this case, the temperature dependence of the integrated spectral weight does actually follow the peak intensity. We define the mean-squared (fluctuating) moment associated with the resonance as  $\langle m_{res}^2 \rangle = 3/(2\pi) \int d(\hbar\omega) \chi''_{res}(\omega) / [1 - \exp(-\hbar\omega/kT)]$ , where  $\hbar$  is Planck's constant divided by  $2\pi$ ,  $k$  is Boltzmann's constant,  $\chi''_{res}(\omega)$  (14, 15) is the resonance part of the acoustic spectrum of Fig. 1, and the factor of 1/2 arises from averaging

$\sin^2(q_d d/2)$  over  $q_d$ . For (123) $O_{6.6}$  and (123) $O_{6.93}$ , our measurements are expressed in absolute units obtained by scaling to the low-temperature measurements performed on both compounds at ISIS (13).

The most obvious feature of Fig. 3, A through C, is that as the doping level and  $T_c$  decrease, there is a progressively larger pretransitional regime above  $T_c$ . Specifically, for the ideally doped sample ( $x = 0.93$ ), the onset of the resonance occurs at a temperature  $T^*$  which almost coincides with  $T_c$ . For  $x = 0.8$  and  $0.6$ ,  $T^*$  increases to approximately  $115 \pm 15$  and  $150 \pm 20$  K, respectively, even while both  $T_c$  and the resonance energy itself are reduced. Thus, the weight of the temperature-dependent resonance joins the long list of properties that show pretransitional behavior in suboptimally doped (123) $O_{6+x}$ . The cross-over temperature  $T^*$  (Fig. 4A) coincides with the temperatures below which the temperature derivatives of the electrical resistivity  $d\rho(T)/dT$  (19, 20) and the Cu nuclear ( $T_1 T$ ) $^{-1}$  relaxation rate (21) reaches a broad maxima. The anomalies occurring at  $T^*$  are generally associated with the opening of a pseudogap in the low-energy spin excitation spectrum, a supposition also supported by neutron scattering data such as those in Fig. 1.

**Fig. 3.** Temperature dependence of the resonance peak intensity (circles) for (A) (123) $O_{6.6}$  at  $\hbar\omega = 34$  meV, (B) (123) $O_{6.8}$  at 39 meV, and (C) (123) $O_{6.93}$  at 40 meV at the (0.5,1.5,1.7) rlu position on triple-axis spectrometers at HFIR. Left axes show intensity normalized to  $\langle m_{res}^2 \rangle$  and right axes to the peak intensity at low temperatures. The error bars in (A) through (C) include only the statistical errors of the triple-axis measurements. The squares in (A) are the integrated  $S_{res}(q,\omega)$  and the triangles in (C) are from (2). The  $T^*$  values are defined as the initial appearance of the resonance. The solid line in (C) below  $T_c$  is a fit using the modified two-fluid model [ $I(T)/I(0) = 1 - (T/T_c)^{3.09}$ ]. (D) The estimated  $d\langle m_{res}^2 \rangle/dT$  for (123) $O_{6+x}$  is from the temperature derivative of the solid lines in (A) through (C). To calculate the absolute magnitude of  $C_J^{res}(x,T)$  using Eq. 2, we assumed  $J = 125$  meV (13),  $\langle m_{res}^2 \rangle = 0.06 \mu_B^2 f.u.^{-1}$ , and 1 mol = 666.15 g for each of the three compositions. Note, we have not considered the uncertainties of  $C_J^{res}(x,T)$  arising from the systematic errors in determining the absolute magnitude of  $\langle m_{res}^2 \rangle$ , due most notably to the ambiguity in removing the nonresonance portion of the signal (Fig. 1A). (E)  $C^{el}(x,T)$  from (9) was converted to SI units using 1 gram-atom unit.  $\equiv 1/(12 + x)$  moles.



According to thermodynamics, a metal undergoes a transition into the superconducting state because such a transition can lower its total free energy,  $F$  (22). The difference in free energy of the system between the normal state, extrapolated to zero temperature ( $F_N$ ) and the superconducting state ( $F_S$ ) is the condensation energy, that is,  $E_C = (F_N - F_S)_{T=0}$ . In principle, the free energy of a system, and therefore  $E_C$ , can be derived from the temperature dependence of  $C^{el}(x,T)$  (8). For (123) $O_{6+x}$ ,  $C^{el}(x,T)$  has been measured by Loram *et al.* (9). The key features of the corresponding data (Fig. 3E) are a sharp jump at  $T_c$  for the optimally doped (123) $O_{6.92}$ , which becomes much suppressed upon reduction of the oxygen content. Although there is less entropy released at  $T_c$ , more seems to be released at temperatures above  $T_c$ , as  $x$  is reduced below its optimal value. Thus, the specific heat tracks the temperature derivative (Fig. 3D) of the spectral weight of the resonance. Just as for the specific heat, decreasing doping reduces the maximum in  $d\langle m_{res}^2 \rangle/dT$  at  $T_c$  and introduces progressively broader high-temperature tails.

In the  $t-J$  model (23), the Hamiltonian of the system consists of a nearest-neighbor

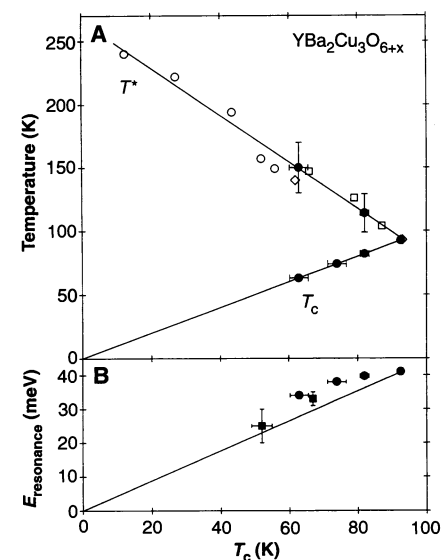


**Fig. 4.** Phase diagram of (123) $O_{6+x}$  which summarizes the results of transport, NMR, and neutron scattering. Because of various methods of oxygenation, slightly different  $T_c$  values are reported for the same nominal doping of (123) $O_{6+x}$ . We avoid this inconsistency by plotting characteristic temperatures as a function of  $T_c$ . (A) The open circles and open squares are temperatures at which  $d\rho(T)/dT$  reaches a broad maximum (19, 20). The open diamonds show the pseudogap temperature  $T^*$  determined from NMR measurements (21). The filled circles locate  $T_c$  and  $T^*$ , where the resonance first appears in our samples. (B) Filled circles show resonance energy versus the transition temperature  $T_c$ . Filled squares are from Fong *et al.* (5). Horizontal error bars are superconducting transition widths. The solid lines are guides to the eye.

hopping ( $t$ ) term accounting for the kinetic energy ( $E_K$ ) of the carriers and a magnetic exchange ( $J$ ) term of the type describing the insulating AF parent compound (24). Magnetic fluctuations with a particular wave vector  $q$  contribute to the exchange energy ( $E_J$ ) via a product with  $J(q)$ , the Fourier transform of the exchange interactions (10). Although magnetic spectra as complicated as those in Fig. 1 will be difficult to describe within such a simple model, the exchange part of the  $t - J$  Hamiltonian does provide a convenient way to quantitatively estimate the effect of magnetic fluctuations on the thermodynamic properties of high- $T_c$  superconductors. For (123)O<sub>6+x</sub>, which has two coupled CuO<sub>2</sub> layers per unit cell, the exchange interactions consist of the nearest-neighbor spin-spin coupling  $J$  in the same CuO<sub>2</sub> plane and the coupling  $J_{\perp}$  between two CuO<sub>2</sub> planes within the unit cell. Since  $J$  is much larger than  $J_{\perp}$  (24), the exchange energy is (10, 11, 25)

$$E_J \approx \frac{3}{(g\mu_B)^2} \left(\frac{a}{2\pi}\right)^2 \int \frac{d(\hbar\omega)}{\pi} \times \int dq_x dq_y \frac{1}{2} J[\cos(q_x a) + \cos(q_y b)] \times \frac{[\chi''_{ac}(q_x, q_y, \omega) + \chi''_{op}(q_x, q_y, \omega)]}{1 - \exp(-\hbar\omega/kT)} \quad (1)$$

where  $g$  is the Lande factor ( $\approx 2$ ) and  $\mu_B$  is the Bohr magneton. Thus, Eq. 1 gives the contribution of the exchange energy to the total energy. Because the heat capacity is the temperature derivative of the total energy, we can estimate how the magnetic fluctuations responsible for the resonance affect the thermodynamic properties of (123)O<sub>6+x</sub> (8, 9). As the resonance grows, more spins fluctuating at the resonance frequency are correlated antiferromagnetically, and the exchange energy is correspondingly reduced. Assuming that the spins accounting for the resonance are not spatially correlated at high temperatures and therefore do not contribute to Eq. 1, the contribution of the exchange energy of the resonance ( $E_J^{res}$ ) to the specific heat, or  $C_J^{res}(x, T)$ , is then

$$C_J^{res}(x, T) \approx \frac{dE_J^{res}}{dT} = -\frac{3}{4\mu_B^2} J \frac{d}{dT} \left( \int \frac{d(\hbar\omega)}{\pi} \frac{\chi''_{res}(\omega)}{1 - \exp(-\hbar\omega/kT)} \right) = -\frac{J}{2\mu_B^2} \frac{d\langle m_{res}^2 \rangle}{dT} \quad (2)$$

Therefore,  $C_J^{res}(x, T)$  is approximately proportional to the temperature derivative of the spectral weight of the resonance, as we already discovered from comparison of our data with the measured specific heat. In deriving Eq. 2 from Eq. 1, we relied on the fact that the resonance is sharply peaked around

( $\pi/a, \pi/b$ ). The contribution of the resonance exchange energy to the heat capacity calculated using Eq. 2 with the measured exchange coupling  $J = 125 \pm 20$  meV for (123)O<sub>6.6</sub> (13) is shown in Fig. 3D (right-hand scale) and can be compared to the measured  $C^{el}(x, T)$  of Loram *et al.* in Fig. 3E (9). The model calculation with no adjustable parameters shows that the resonance can provide enough temperature-dependent exchange energy to yield the superconducting anomaly in the specific heat (26). This suggests that a large part of the specific heat near  $T_c$  and its associated entropy are due to spin fluctuations.

Clearly, the measured specific heat includes contributions other than that due to the exchange energy of the resonance ( $E_J^{res}$ ). Although we included the most obvious temperature-dependent feature in our calculation, the temperature evolution of the remainder of the spin excitation spectrum is neglected. Most notably, we ignored the formation of the spin pseudogap below  $T^*$  and spin gap below  $T_c$ , both of which could increase  $E_J$ . Further, we have not considered the contribution of  $E_K$  to  $C^{el}(x, T)$ . For superconductors,  $E_K$  is expected to increase from the normal to the superconducting state (10). Both this effect and spin (pseudo)gap formation could partially compensate for the reduction of  $E_J$  because of the appearance of the resonance. Such compensation might explain why the area of the calculated  $C_J^{res}(x, T)$  anomaly is considerably larger than that of the  $C^{el}(x, T)$  measurement.

In the next few years, the contributions missing from our analysis should become calculable using better neutron and optical conductivity data, which would provide the necessary information on the temperature-dependent magnetic exchange and kinetic energy terms, respectively. It would also be of considerable interest to make further model calculations to estimate the change in the resonance exchange energy between the normal and superconducting states at zero temperature, and hence, the resonance exchange energy contribution to the condensation energy (10, 11). Unfortunately, this comparison is difficult because the normal state  $S(q, \omega)$  must be extrapolated to zero temperature. This cannot be done reliably with the our data here and presents a challenge for the future.

In summary, we show that a pseudogap regime bounded by a temperature  $T^* > T_c$  determined from transport, NMR, and thermodynamic measurements can be associated with the appearance of the resonance peak and the suppression of the low-frequency response in the magnetic excitation spectrum. Our complete spectra allow us to establish the weight of the resonance relative to that of other spectral features. A simple calculation of the exchange energy using the measured temperature dependence of the resonance shows that spin fluctuations can account for a

large part of the electronic specific heat near the superconducting transition.

### References and Notes

1. J. Rossat-Mignod *et al.*, *Physica C* **185**, 86 (1991).
2. H. A. Mook, M. Yethiraj, G. Aeppli, T. E. Mason, T. Armstrong, *Phys. Rev. Lett.* **70**, 3490 (1993).
3. H. F. Fong *et al.*, *ibid.* **75**, 316 (1995).
4. P. Dai, M. Yethiraj, H. A. Mook, T. B. Lindemer, F. Doğan, *ibid.* **77**, 5425 (1996).
5. H. F. Fong, B. Keimer, D. L. Millis, I. A. Aksay, *ibid.* **78**, 713 (1997).
6. P. Bourges *et al.*, *Phys. Rev. B* **56**, R11439 (1997).
7. B. Batlogg, C. W. Chu, W. K. Chu, D. V. Gubser, K. A. Muller, Eds., *Proceedings of the 10th Anniversary High-Temperature Superconductivity Workshop on Physics, Materials, and Applications*, Houston, TX, 12 to 16 May 1996 (World Scientific, Singapore, 1996).
8. J. W. Loram, K. A. Mirza, P. F. Freeman, *Physica C* **171**, 243 (1990).
9. J. W. Loram, K. A. Mirza, J. R. Cooper, W. Y. Liang, J. M. Wade, *J. Supercond.* **7**, 243 (1994).
10. D. J. Scalapino and S. R. White, *Phys. Rev. B* **58**, 8222 (1998).
11. E. Demler and S. C. Zhang, *Nature* **396**, 733 (1998).
12. See, for example, G. Aeppli, S. M. Hayden, T. G. Perring, *Phys. World* **10**, 33 (December 1997).
13. S. M. Hayden *et al.*, *Physica B* **241-243**, 765 (1998).
14. We used the elastic incoherent scattering from a vanadium standard under the same experimental conditions to put the two-dimensional wave vector-integrated or local-susceptibility  $\chi''(\omega) = (a/2\pi)^2 \int_{BZ} \chi''(q_x, q_y, \omega) dq_x dq_y$  from (123)O<sub>6+x</sub> on an absolute scale [for example, (16)]. Although at low frequencies,  $\chi''(q, \omega)$  for (123)O<sub>6.6</sub> has been shown to peak at wave vector positions incommensurate from the underlying crystallographic lattice in the low-temperature superconducting state (17, 18), we only used a Gaussian convolved with the instrumental resolution to carry out the momentum integration within the scattering plane [see figure 6 of (13)]. The poor out-of-plane resolution of the instrument means that the integration of the magnetic intensity over momentum transfer perpendicular to the scattering plane is carried out automatically. The validity of such procedure to obtain  $\chi''(\omega)$  has been confirmed by integrating the two-dimensional images of  $\chi''(q_x, q_y, \omega)$  at 24 and 34 meV (18).
15. It is convenient to split the magnetic response into two parts  $\chi''(q, \omega) = \chi''_{ac}(q_x, q_y, \omega) \sin^2(q_z d/2) + \chi''_{op}(q_x, q_y, \omega) \cos^2(q_z d/2)$ , where  $d$  is the spacing between nearest-neighbor CuO planes.
16. S. M. Hayden *et al.*, *Phys. Rev. Lett.* **76**, 1344 (1996).
17. P. Dai, H. A. Mook, F. Doğan, *ibid.* **80**, 1738 (1998).
18. H. A. Mook *et al.*, *Nature* **395**, 580 (1998).
19. T. Ito, K. Takenaka, S. Uchida, *Phys. Rev. Lett.* **70**, 3995 (1993).
20. B. Wuyts, V. V. Moshchalkov, Y. Bruynseraede, *Phys. Rev. B* **53**, 9418 (1996).
21. M. Takigawa *et al.*, *ibid.* **43**, 247 (1991).
22. J. R. Shrieffer, *Theory of Superconductivity* (Benjamin, New York, 1964).
23. F. C. Zhang and T. M. Rice, *Phys. Rev. B* **37**, 3759 (1988).
24. See, for example, S. M. Hayden, G. Aeppli, T. G. Perring, H. A. Mook, F. Doğan, *ibid.* **54**, R6905 (1996).
25. Note that our susceptibility  $\chi$  is defined as  $1/3(\chi_{xx} + \chi_{yy} + \chi_{zz})$  while  $\chi_{+-}$  is used in (11). We wish to thank E. Demler for pointing this out and for many discussions about condensation energy in the high- $T_c$  superconductors.
26.  $C_J^{res}(x, T)$  is the resonance contribution to the  $C^{el}(x, T)$ , not  $C^{el}(x, T)$  itself. Therefore, one should only compare  $C_J^{res}(x, T)$  to the change in  $C^{el}(x, T)$  above the sloped background.
27. S. Shamoto, M. Sato, J. M. Tranquada, B. J. Sternlieb, G. Shirane, *Phys. Rev. B* **48**, 13817 (1993).
28. We thank B. Batlogg, E. Demler, R. S. Fishman, J. W. Loram, D. Morr, D. Pines, D. J. Scalapino, and S. C. Zhang for stimulating discussions. The work at Oak Ridge National Laboratory was supported by the U.S. Department of Energy under contract DE-AC05-96OR22464 with Lockheed Martin Energy Research Corporation.

6 January 1999; accepted 20 April 1999